Progress In Electromagnetics Research M, Vol. 51, 19–31, 2016

Retrieval of Refractivity Profile with Ground-Based Radio Occultation by Using an Improved Harmony Search Algorithm

Mu-Min Chiou and Jean-Fu Kiang*

Abstract—A ground-based radio occultation (RO) technique is proposed to retrieve the atmospheric refractivity profile around a specific region at a higher sampling rate than conventional space-based RO techniques, making it more suitable for regional weather studies. A harmony search (HS) algorithm with ensemble consideration (HS-EC) based on atmospheric physics is proposed to retrieve the refractivity profile more efficiently without being trapped in suboptimal solutions. The highest altitude of profile is extended to 95 km from 40 km adopted in conventional ground-based RO techniques, leading to more accurate results.

1. INTRODUCTION

The height profile of refractivity used to be retrieved by using space-based radio occultation (RO) technique [1, 2], where excess phase-paths of GPS signals received at low-earth orbit (LEO) satellites and the bending angles of ray paths were used to reconstruct a height profile of refractivity via Abel transform [3, 4]. Global coverage of refractivity profiles is useful to predict weather conditions in the troposphere and the lower stratosphere [5, 6], to study heavy precipitation [7], Arctic atmosphere [8], severe weather events [9, 10], and over-the-horizon communication channels [11].

The space-based RO technique becomes less accurate in the lower troposphere, especially when a super-refraction (SR) layer is present [12], which happens frequently above sea surfaces [13]. Currently available space-based RO missions can provide only relatively sparse data for any specific region of interest [14], which is not sufficient for regional weather studies. A tomography technique was applied to retrieve meteorological profiles in the atmosphere by deploying a dense network of GPS receivers [15]. However, to monitor the temporal and spatial variations around a specific region demands even more receivers [16].

Ground-based RO technique was proposed for regional weather studies, which demanded a high sampling rate [14, 17]. A practical ground-based RO technique can be implemented at a specific site, by installing a receiver on building roof, vehicle or ship [18]. A ray-tracing model was applied to retrieve the atmospheric refractivity profile from the measurement data of GPS tropospheric delays [19]. In [20], a three-level model was proposed to characterize the ducting conditions near coast. Temporal and spatial variations in temperature, pressure and water vapor create a volatile refractivity profile, making its retrieval a challenging task. In [21], GPS signals at a specific ground-based receiver were used to retrieve height profile of maritime refractivity by using an artificial neural network technique, which was validated by measurement data on the coast of the Yellow sea.

In [18], an exhaustive search (ES) method was applied to retrieve the refractivity profile from the boundary layer up to 10 km above ground, with data from a single ground-based GPS receiver. The computational time of the exhaustive search method grows exponentially with the number of

Received 25 May 2016, Accepted 24 August 2016, Scheduled 14 October 2016

* Corresponding author: Jean-Fu Kiang (jfkiang@ntu.edu.tw).

The authors are with the Department of Electrical Engineering and the Graduate Institute of Communication Engineering, National Taiwan University, Taipei, Taiwan.

unknowns [22]. To reduce the size of search space, variable searching steps were taken at different heights, and the data of the Constellation Observing System for Meteorology, Ionosphere, and Climate (COSMIC) mission from 2007 to 2011 were used as prior information [23]. A harmony search (HS) algorithm, inspired by the improvisation process of Jazz musicians, was proposed to search for the optimal solution more efficiently [24]. To avoid being trapped in local optimal solutions, ensemble consideration was implemented to constrain the solution vector to resemble a preferred pattern.

In this work, we will first demonstrate that more accurate data of excess phase-path are critical to the effectiveness of a ground-based RO technique. In order to obtain more accurate excess phase-paths, the upper bound of integration assumed in the ray-tracing model should be increased. An HS algorithm with ensemble consideration (HS-EC) based on atmospheric physics is proposed to retrieve the refractivity profile, which contains more unknowns than the conventional exhaustive search method can handle at a reasonable computational load.

This paper is organized as follows. A ray-tracing model is briefly reviewed in Section 2. The significance of integration upper bound on computing the excess phase-path is analyzed in Section 3. The HS-EC algorithm based on atmospheric physics is presented in Section 4. Simulation results are discussed in Section 5. Finally, some conclusions are drawn in Section 6.

2. RAY-TRACING MODEL IN GROUND-BASED RO

In this section, some basic concepts of ray tracing and the retrieval algorithm applied in ground-based RO are briefly reviewed. Figure 1 shows the geometry of a ray path in a scenario of ground-based radio occultation [20], where A_1 and A_2 represent a GPS receiver on the ground and a GPS satellite, respectively; with their distances to the Earth center being r_1 and r_2, respectively.

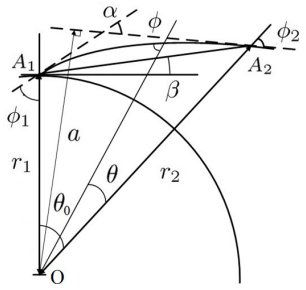

Figure 1. Geometry of ray path in ground-based radio occultation [20].

If the atmospheric profile is approximated as a function of r only, the phase-path between points A_1 and A_2 is determined as

$$S = \int_{A_1}^{A_2} n d\ell, \tag{1}$$

where $d\ell = \sqrt{dr^2 + r^2 d\theta^2} = dr/\cos\phi$ is a differential length along the ray path, and n is the refractive index. In practice, a refractivity is defined as $N = 10^6 \times (n-1)$, which can be empirically estimated as [18]

$$N = k_1 \frac{P}{T} + k_2 \frac{P_w}{T^2}, \tag{2}$$

where $k_1 = 77.6$ (N-unit $\times$ K/hPa) and $k_2 = 3.73 \times 10^5$ (N-unit $\times$ K^2/hPa); P (hPa), P_w (hPa) and T (K) are the atmospheric pressure, water-vapor pressure and temperature, respectively.

A ray path in a spherically symmetric medium follows the Bouger's law, $a = nr\sin\phi$, where a is a constant impact parameter associated with the ray path. Thus, Eq. (1) can be represented as

$$S = \int_{r_1}^{r_2} \frac{rn^2}{\sqrt{r^2n^2 - a^2}} dr = \int_{x_1}^{x_2} \frac{x\,[1 - (x/n)dn/dx]}{\sqrt{x^2 - a^2}} dx, \tag{3}$$

where $x = rn$ is called the refractional radius. The phase-path along a straight line between A_1 and A_2, as if they were in vacuum, can be determined as

$$S_0 = \sqrt{r_1^2 + r_2^2 - 2r_1 r_2 \cos\theta_0}, \tag{4}$$

where θ_0 is the angle span between $\overline{OA_1}$ and $\overline{OA_1}$.

An excess phase-path is defined as [20]

$$\Delta S = S - S_0, \tag{5}$$

and the elevation angle β is determined as

$$\beta = \tan^{-1} \frac{r_2 \cos\theta_0 - r_1}{r_2 \sin\theta_0}. \tag{6}$$

As the satellite moves in its orbit, many ray paths are established between A_1 and A_2, with each ray path associated with an elevation angle β and an excess phase-path ΔS. The information of $N(h)$ is embedded in these pairs of $(\Delta S, \beta)$'s, which can be transformed to a functional form of $\Delta S(\beta)$ by applying a cubic-spline interpolation [20]. The retrieved refractivity can be determined by fitting the modeled excess phase-path $\Delta S^{\mathrm{mod}}(\beta)$ with the measured excess phase-path $\Delta S^{\mathrm{mea}}(\beta)$ in the least-square sense as

$$N^{\mathrm{re}}(h) = \arg \min_{N(h)} \left\{ \sum_{m=1}^{M_o} \left[\Delta S^{\mathrm{mea}}(\beta_m) - \Delta S^{\mathrm{mod}}(\beta_m) \right]^2 \right\}, \tag{7}$$

where M_o is the number of measurement data, and $h = r - R_e$ is the height above ground.

The effects of horizontal refractivity gradient, multipath and atmospheric diffraction are neglected at $\beta > 3^\circ$. When $\beta > 5^\circ$, the variation of ΔS over different refractivity profiles becomes insignificant [25]. Hence, the range of elevation angle in this work is chosen to be $3^\circ \leq \beta \leq 5^\circ$ [18].

3. EFFECT OF UPPER BOUND ON EXCESS PHASE-PATH

In this section, the effect of upper bound in the integral is studied, with practical atmospheric profiles. Figure 2 shows the geometry of a ray path for computing the phase-path from A_1 to A_2 via A_u, above which the refractive index is approximated as one. The point A_u is at a distance of r_u from the Earth center, or is at a height of $h_u = r_u - r_1$ above ground. Let the phase-path between A_1 and A_u be S_{1u}, and that between A_u and A_2 be S_{u2}. Thus, the phase-path integration in Eq. (3) is divided to two parts as

$$S = \int_{x_1}^{x_u} \frac{x\,[1 - (x/n)dn/dx]}{\sqrt{x^2 - a^2}} dx + \int_{x_u}^{x_2} \frac{x\,[1 - (x/n)dn/dx]}{\sqrt{x^2 - a^2}} dx, \tag{8}$$

where the two terms on the right-hand side are S_{1u} and S_{u2}, respectively, and $x_\alpha = n_\alpha r_\alpha$ is the refractional radius at A_α, with $\alpha = 1, 2, u$. Since the refractive index above h_u is approximated as one, S_{u2} can be approximated as

$$S_{\mathrm{oa}} = \sqrt{x_2^2 - a^2} - \sqrt{x_u^2 - a^2}.$$

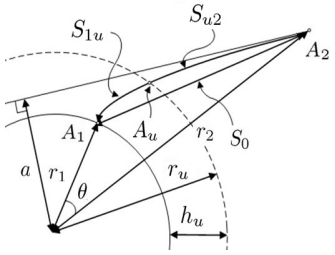

Figure 2. Geometry of ray path from A_1 via A_u to A_2, for computing the phase-path.

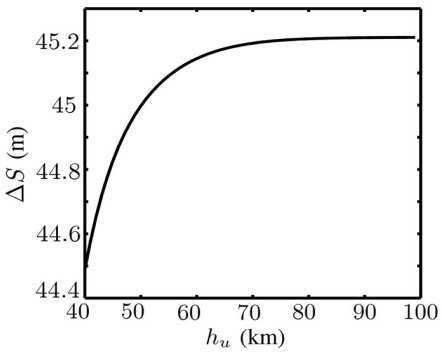

Figure 3. Profile of excess phase-path ΔS, at 00:00 UTC, Jan. 1, 2014, (23.5°N, 120°E), $r_1 = 6,400$ km, $r_2 = 26,600$ km, $a = 6,396.984$ km.

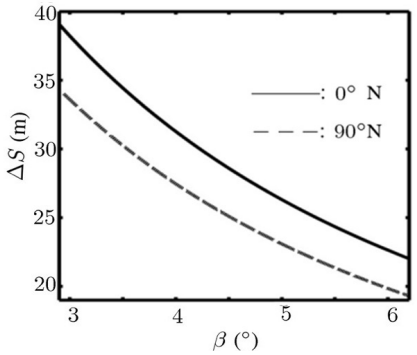

Figure 4. Excess phase-path versus elevation angle in two refractivity profiles at latitudes 0° and 90°N, respectively, derived from the zonal average pressure and temperature of the CIRA86aQ_UoG model in January [26].

By using Eqs. (4), (5) and (8), a relation between the excess phase-path ΔS and h_u is obtained, as shown in Figure 3. Note that $\Delta S(h_u)$ increases with h_u and approaches a constant when $h_u > 90$ km.

Figure 4 shows the excess phase-path as a function of elevation angle, in two refractivity profiles at latitudes 0° and 90°N, respectively [26]. The difference between these two excess phase-paths is about 5 m at all elevation angles. Other parameters like slant delays and slant factors involved in a typical ray-tracing method were discussed in [27]. However, the minimum altitude required to acquire accurate phase-paths was not conclusive for ground-based RO techniques, and 40 km was frequently adopted as the upper bound of integration for computing phase-paths [18].

Figure 3 shows that as h_u is changed from 40 km to 90 km, the excess phase-path is changed by about 0.7 m, which is about 1/7 of the difference between the two curves in Figure 4. This implies if h_u is set to 40 km, one may not be able to tell apart the excess phase-paths in two different refractivity profiles. In this work, the upper bound is raised to 95 km, above which the refractive index is much closer to one than at 40 km above ground.

The air pressure, water-vapor pressure and temperature can be derived from the European Centre for Medium-Range Weather Forecast (ECMWF) model [28]. However, the ECMWF model and the COSMIC mission [23] provide atmospheric data only up to 50 km above ground. Hence, the CIRA86aQ_UoG model [26] and the MSIS-E-90 model [29] are adopted to provide the pressure and temperature profiles up to the altitude of 95 km.

4. HARMONY SEARCH ALGORITHM WITH ENSEMBLE CONSIDERATION ON ATMOSPHERIC PHYSICS

In this Section, the HS-EC algorithm tailored for ground-based RO missions is presented.

4.1. Harmony Search Algorithm

The harmony search (HS) algorithm updates the solution set stored in a harmony memory (HM), which can be represented as [24, 30]

$$\mathrm{HM} = \begin{bmatrix} N_{11} & N_{21} & \dots & N_{\mathrm{HMS}1} \\ N_{12} & N_{22} & \dots & N_{\mathrm{HMS}2} \\ \vdots & \vdots & \dots & \vdots \\ N_{1M} & N_{2M} & \dots & N_{\mathrm{HMS}M} \end{bmatrix},$$

where M is the number of musicians, HMS is the harmony-memory size, N_{nm} is the nth harmony of the mth musician, and each column of the HM matrix is called a harmony vector. Typically, a harmony

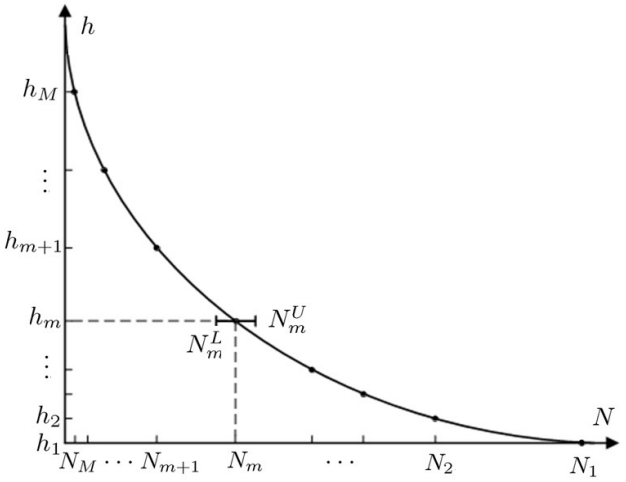

Figure 5. Refractivity profile $\{N_m\}$ sampled at altitudes $\{h_m\}$, with $1 \le m \le M$.

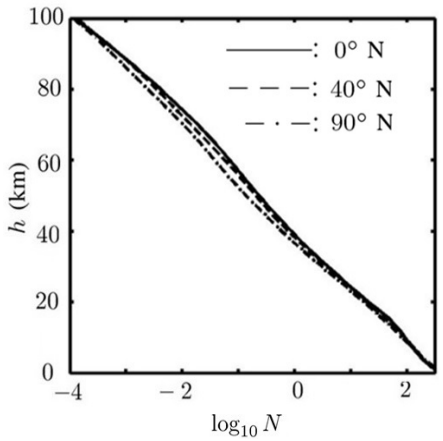

Figure 6. Refractivity profiles in January derived from the CIRA86aQ_UoG model.

vector having a smaller object function value is placed before those having larger object function values. Figure 5 shows an example of refractivity profile, which is represented by the best harmony vector to be, $\bar{N} = [N_1, N_2, \ldots, N_M]^t$, where N_m is the refractivity at height h_m.

Figure 6 shows three refractivity profiles over the heights from 0 to 100 km, which are obtained by applying Eq. (2), where the zonal average pressure and temperature are derived from the CIRA86aQ_UoG model [26]. These curves can be fit with logarithmic-like functions as [18]

$$N(h) = N_m \exp\left\{-\frac{h - h_m}{h_{m+1} - h_m} \ln \frac{N_m}{N_{m+1}}\right\}, \quad h_m \le h \le h_{m+1}.$$

In each improvisation, the HS algorithm is implemented in five steps, which are briefly described as follows.

Step 1, random selection process:

In the beginning of the ℓth improvisation, a new harmony vector $\bar{N}^{(\ell)}$ is generated, with its mth entry picked from an interval as

$$N_m^{(\ell)} = U(N_m^L, N_m^U), \tag{9}$$

where $U(\alpha, \beta)$ represents a uniform distribution over the interval (α, β); N_m^L and N_m^U are the lower and upper bounds, respectively, of N_m, which are also marked in Figure 5.

Step 2, memory consideration process:

An alternative new harmony vector $\bar{N}^{(\ell)}$ is generated as

$$N_m^{(\ell)} = N_{pm}, \tag{10}$$

where N_{pm} is the pmth entry in the harmony memory, with

$$p = \lfloor U^2(0,1) \times \mathrm{HMS} \rfloor + 1, \tag{11}$$

where $\lfloor r \rfloor$ means the integer part of a positive real number r. Steps 1 and 2 are executed with probabilities of 1-HMCR and HMCR, respectively.

Step 3, pitch adjustment process:

The value of $N_m^{(\ell)}$ is pitch-adjusted as

$$N_m^{(\ell)} = N_{pm} + U(-1,1) \times \mathrm{FW}_m, \tag{12}$$

with a probability of PAR, where FW_m is the fret width of the mth musician, which is about 1% to 10% of $N_m^U - N_m^L$ [24].

Step 4, memory update process:

If $\bar{N}^{(\ell)}$ bears a smaller object function value than the worst harmony in the HM, the latter will be replaced with $\bar{N}^{(\ell)}$.

Step 5, accidentaling process:

If $\bar{N}^{(\ell)}$ is the best within the HM, it will be pitch-adjusted as

$$N_m^{\rm ac} = N_m^{(\ell)} + U(-1,1) \times {\rm FW}_m, \quad 1 \le m \le M. \tag{13}$$

If $\bar{N}^{\rm ac}$ bears a smaller object function value than the worst harmony in the HM, the latter will be replaced with $\bar{N}^{\rm ac}$. The HS algorithm stops as the iteration index ℓ reaches an upper bound K.

4.2. HS Algorithm with Ensemble Consideration

Refractivities N_{m+1} and N_m, at adjacent heights, are strongly correlated because the atmospheric variables P, T and P_w that determine the refractivity do not change drastically over a small height range. This fact can be used to guide the HS algorithm from converging to suboptimal solutions. It is implemented in the form of ensemble consideration (EC), in which the refractivities at adjacent height intervals, $\bar{N}_m^{(\ell)}$ and $\bar{N}_{m+1}^{(\ell)}$, are constrained to resemble the so called ensemble-consideration refractivities $\bar{N}_m^{\rm EC}$ and $\bar{N}_{m+1}^{\rm EC}$, respectively. The latter are derived by imposing atmospheric physics as in Step 1a below.

Figure 7 shows a flowchart of the HS-EC algorithm, in which the ensemble consideration is implemented in the processes of random selection, memory consideration, pitch adjustment and accidentaling. The processes enclosed in the dashed rectangle are used to generate a new harmony vector $\bar{N}^{(\ell)}$, and K is an upper bound of iteration index ℓ. The four steps of the HS-EC algorithm are described as follows.

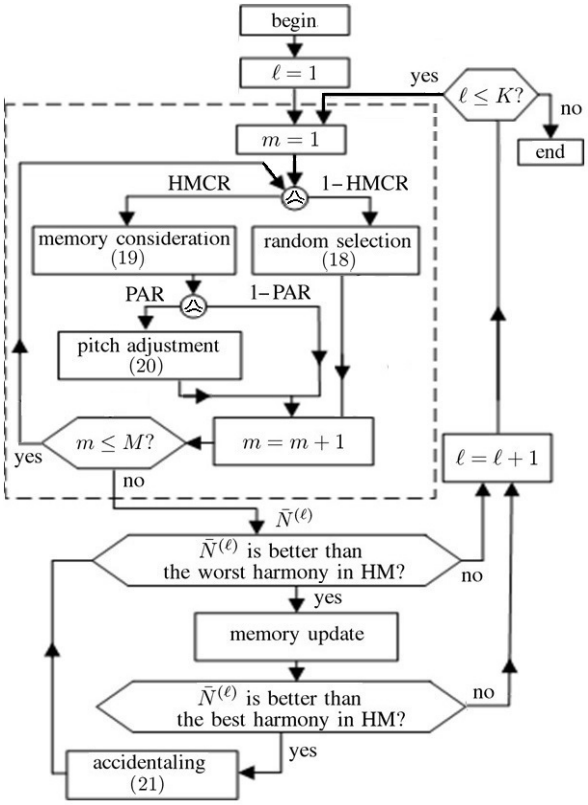

Figure 7. Flow-chart of HS-EC algorithm.

Step 1a, random selection process:

The measurement data on the ground is taken as N_1, and the other $\bar{N}^{(\ell)}$'s are generated as

$$N_m^{(\ell)} = N_{m-1}^{(\ell)} \frac{N_m^{\mathrm{EC}}}{N_{m-1}^{\mathrm{EC}}} + c_1 \times U(-1,1) \times \left(N_m^U - N_m^L\right), \quad 2 \le m \le M, \tag{14}$$

where c_1 is a weighting coefficient, with a normal range from 0.01 to 0.1 [24]. Choosing a smaller c_1 will make $N_m^{(\ell)}$ closer to the ensemble-consideration refractivity profile in $[h_{m-1}, h_m]$. In the simulations, c_1 is decreased linearly from an initial value c_{10} at $\ell = 1$ to zero at $\ell = K$.

The ensemble-consideration refractivity profile $\bar{N}^{\mathrm{EC}}$ is derived by using Eq. (2), with the temperature $T(h)$, pressure $P(h)$ and water vapor $P_w(h)$ estimated as [26, 31]

$$\begin{aligned} T(h) &= T^C(h) - T_0^C + T_0^{\mathrm{mea}}, \\ P(h) &= P_0^{\mathrm{mea}} \exp\left\{-\frac{g m_a}{R} \int_0^h \frac{dh}{T}\right\}, \\ P_w(h) &= P_w^C(h) \frac{P_{w0}^{\mathrm{mea}}}{P_{w0}^C}, \end{aligned}$$

where $T^C(h)$ and T_0^C are the temperature profile and the temperature on the ground, respectively, derived from the CIRA86aQ_UoG model; T_0^{mea} is the measured temperature on the ground, P_0^{mea} the measured pressure on the ground, $R = 8.31451 \times 10^4\,\mathrm{cm^3hPa/mole/K}$ the atmospheric constant, and $m_a = 0.028966\,\mathrm{kg/mole}$ the molecular weight averaged over N_2, O_2, Ar and CO_2 in a standard model; $P_w^C(h)$ and P_{w0}^C are derived from the CIRA86aQ_UoG model, and P_{w0}^{mea} is the water-vapor pressure measured on the ground.

Step 2a, memory consideration process:

The mth entry of $N^{(\ell)}$ is alternately generated as

$$N_m^{(\ell)} = N_{m-1}^{(\ell)} \frac{N_{pm}}{N_{p(m-1)}}, \tag{15}$$

where p is determined by using Eq. (11). Steps 1a and 2a are executed with probabilities of 1-HMCR and HMCR, respectively.

Step 3a, pitch adjustment process:

The value of $N_m^{(\ell)}$ is pitch-adjusted as

$$N_m^{(\ell)} = N_m^{(\ell)} + c_1 \times U(-1,1) \times \left(N_m^U - N_m^L\right), \tag{16}$$

with a probability of PAR.

Step 5a, accidentaling process:

If $\bar{N}^{(\ell)}$ is the best within the HM, it will be pitch-adjusted as

$$N_m^{\mathrm{ac}} = N_m^{(\ell)} + c_2 \times U(-1,1) \times \left(N_m^U - N_m^L\right), \quad 1 \le m \le M, \tag{17}$$

where c_2 is a weighting coefficient to fine-tune the best candidate solution. The value of c_2 is usually smaller than c_1 and is decreased linearly from c_{20} at $\ell = 1$ to zero at $\ell = K$. The idea of decreasing c_1 and c_2 is to encourage exploration in the early stage while accelerate convergence in the late stage [32].

In practice, a negative refractivity may occur at high altitudes due to the random term $c_1 \times U(-1,1) \times (N_m^U - N_m^L)$ in Eqs. (14) and (16), because the modeled refractivity generated with Eqs. (14) and (15) decreases moronically with height, and a small N_m^ℓ tends to generate an even smaller N_q^ℓ with $q \ge m+1$. This issue can be resolved by imposing the ensemble consideration.

5. SIMULATIONS AND DISCUSSIONS

In the simulations, it is assumed that the GPS satellites move at an orbital height of 20,200 km, with an inclination angle of 55°, and the receiver is placed on the ground. The target refractivity profile (N^{tar}) is derived by using (2), where T and P are derived from the MSIS-E-90 model and P_w is derived

from the ECMWF model. The maximum error of excess phase-path in ground-based measurements was about 15 cm [20, 33]. In this work, the simulated excess phase-path is the sum of the actual excess phase-path (ΔS) and a Gaussian noise with zero mean and standard deviation of $10^{-3}\Delta S$ [20].

To evaluate the quality of reconstructed refractivity profile, a root-mean-square (rms) percentage error is defined as

$$\varepsilon = 100 \times \sqrt{\frac{1}{h_b - h_a} \int_{h_b}^{h_a} \frac{|N^{\rm re}(h) - N^{\rm tar}(h)|^2}{|N^{\rm tar}(h)|^2} dh}, \tag{18}$$

where h_a and h_b are chosen to cover the troposphere and the lower stratosphere. The tropopause between the troposphere and stratosphere lies at the height of about 18 km near the equator, about 10 km at mid-latitudes, and about 8 km at the poles.

In applying the HS algorithm, the number of unknowns in a profile was below 40 [34]. In order to retrieve the refractivity profile from ground up to 95 km at height, without involving too many unknowns, the refractivity profile is sampled with a finer resolution at lower altitudes and a coarser resolution at higher altitudes. Table 1 lists two altitude schemes, with Δh indicating altitude resolution. In scheme 1, the sampling interval is 0.5 km in $0 \le h \le 10$ km, 2 km in $10 \le h \le 20$ km, 5 km in $20 \le h \le 75$ km, and 10 km in $75 \le h \le 95$ km, adding up to 39 height levels. In scheme 2, the sampling interval is 1 km in $0 \le h \le 10$ km, 2 km in $10 \le h \le 20$ km, 5 km $20 \le h \le 75$ km, and 10 km in $75 \le h \le 95$ km, adding up to 29 height levels.

Table 1. Two altitude schemes adopted in simulations.

altitude scheme 1 (39 levels)				
altitude range (km)	0–10	10–20	20–75	75–95
Δh (km)	0.5	2	5	10
altitude scheme 2 (29 levels)				
altitude range (km)	0–10	10–20	20–75	75–95
Δh (km)	1	2	5	10

5.1. Comparison between HS-EC and ES

Firstly, the HS-EC algorithm will be compared with the conventional exhaustive search (ES) method, with altitude scheme 2 listed in Table 1. A refractivity profile at (23°N, 120°E), 00:00 UTC, Jan. 1, 2013 is generated as the target refractivity profile, $N^{\rm tar}$. The temperature and pressure profiles are derived from the MSIS-E-90 model, and the water-vapor pressure profile is derived from the ECMWF model.

Table 2 lists the rms percentage error averaged over 100 realizations by using the ES [18] and the HS-EC algorithms, respectively, and each is tested with different h_u's. The parameters used in the HS-EC algorithm are HMS = 20, HMCR = 0.9, PAR = 0.7, $c_{10} = 0.1$ and $c_{20} = 0.01$.

Table 2. Average rms percentage error of ES and HS-EC.

algorithm	ES [18]	HS-EC	HS-EC
altitude scheme	2	2	1
ε ($h_a = 0$, $h_b = 10$ km); $h_u = 40$ km	2.67	2.37	2.08
ε ($h_a = 10$ km, $h_b = 20$ km); $h_u = 40$ km	4.01	3.64	3.45
ε ($h_a = 0$, $h_b = 10$ km); $h_u = 95$ km	2.45	2.06	1.84
ε ($h_a = 10$ km, $h_b = 20$ km); $h_u = 95$ km	3.72	3.56	3.23

It is observed that the average rms percentage error is higher with ($h_a = 10\,\text{km}$, $h_b = 20\,\text{km}$) than that with ($h_a = 0$, $h_b = 10\,\text{km}$). The refractivity decreases with height, and a fixed absolute error ($\left|N^{\text{re}}(h) - N^{\text{tar}}(h)\right|$) will result in a higher rms percentage error according to the definition in Eq. (18). By increasing h_u from 40 km to 95 km, with altitude scheme 2, the average rms percentage error slightly decreases from 2.67 to 2.45 by using the ES method, and from 2.37 to 2.06 by using the HS-EC algorithm. The retrieved profile with $h_u = 95\,\text{km}$ appears more accurate than that with $h_u = 40\,\text{km}$ because more accurate excess phase-paths are available in the former case by including information from the upper atmosphere. If altitude scheme 1 is adopted, which defines a finer vertical resolution in the altitude range of 0–10 km, the average rms percentage error by using the HS-EC algorithm with $h_u = 95\,\text{km}$ can be further reduced to 1.84.

Given the number of excess phase-paths (M) required in one mission, the computational load of the ES method is on the order of q^M, where q is the number of candidate values at each height interval, usually larger than 10 [18]. As a result, the computational load with altitude scheme 1 will become too huge to be practical. That could be the reason why the ES method was often used with height intervals larger than 1 km [18]. On the other hand, the computational load of the HS or the HS-EC algorithm is on the order of $20,000$, which is much smaller than q^M.

5.2. Comparison between HS-EC and HS

Figure 8(a) shows the retrieved refractivity N^{re} and error $N^{\text{re}} - N^{\text{tar}}$ by using the HS algorithm, with the parameters HMS = 20, HMCR = 0.95, PAR = 0.5 and $K = 20,000$. The retrieved refractivity profile appears non-monotonical at heights around 1.8, 2.1 and 4.2 km, respectively, indicating that N^{re} could be a suboptimal solution.

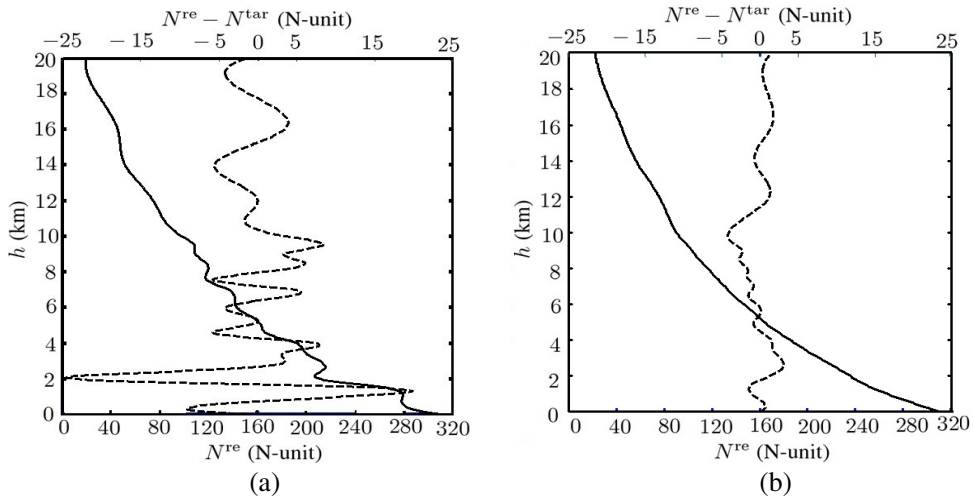

Figure 8. Retrieved refractivity N^{re} (———) and error $N^{\text{re}} - N^{\text{tar}}$ (− − −) by using (a) HS algorithm and (b) HS-EC algorithm.

Figure 8(b) shows the retrieved refractivity profile and the error by using the HS-EC algorithm, with the parameters HMCR, PAR, HMS and K the same as in the HS algorithm, and the tuning parameters are $c_{10} = 0.1$ and $c_{20} = 0.01$. The retrieved refractivity profile appears monotonical, and the errors are smaller than those in Figure 8(a).

In the HS-EC algorithm, the candidate refractivity profile is constrained to resemble $\bar{N}^{\text{EC}}$, which is realized with atmospheric physics information available from a standard atmosphere model and measurement data on the ground. Without this mechanism, the HS algorithm is easier to converge to a suboptimal solution, especially when the number of height intervals is large.

5.3. Fine-Tune of HS Parameters

The accuracy of solution obtained with the HS-EC algorithm can be further increased by fine-tuning the relevant parameters. Table 3 lists the average rms percentage error over 100 realizations, with $K = 20,000$, $c_{10} = 0.1$, $c_{20} = 0.01$, along with different combinations of HS parameters. It is concluded that choosing HMS = 100, HMCR = 0.9 or 0.95, and PAR = 0.7 will achieve smaller rms percentage errors.

Table 3. Effects of HMS, HMCR and PAR on average rms percentage error, $h_a = 0$, $h_b = 10\,\text{km}$.

HMS = 20	HMCR			
	0.7	0.8	0.9	0.95
PAR = 0.3	2.14	2.11	2.04	1.99
PAR = 0.5	1.92	1.94	1.94	1.92
PAR = 0.7	1.88	1.89	1.84	1.78

HMS = 50	HMCR			
	0.7	0.8	0.9	0.95
PAR = 0.3	2.06	2.02	1.96	1.98
PAR = 0.5	1.86	1.85	1.84	1.88
PAR = 0.7	1.83	1.80	1.75	1.76

HMS = 100	HMCR			
	0.7	0.8	0.9	0.95
PAR = 0.3	1.97	1.95	1.89	1.91
PAR = 0.5	1.81	1.80	1.78	1.83
PAR = 0.7	1.74	1.77	1.67	1.71

Table 4 lists the average rms percentage error over 100 realizations, with $K = 20,000$, HMS = 100, HMCR = 0.9, PAR = 0.7, along with different combinations of c_{10} and c_{20}. Smaller rms percentage errors can be achieved with $0.04 \le c_{10} \le 0.1$ and $0.007 \le c_{20} \le 0.02$.

Table 4. Effects of c_{10} and c_{20} on average rms percentage error, $h_a = 0$, $h_b = 10\,\text{km}$.

	c_{10}					
	0.005	0.01	0.04	0.07	0.1	0.2
$c_{20} = 0.001$	1.89	1.81	1.75	1.74	1.75	1.79
$c_{20} = 0.004$	1.84	1.76	1.72	1.73	1.73	1.74
$c_{20} = 0.007$	1.83	1.73	1.71	1.68	1.69	1.72
$c_{20} = 0.01$	1.84	1.72	1.70	1.69	1.67	1.70
$c_{20} = 0.02$	1.86	1.73	1.71	1.72	1.69	1.74
$c_{20} = 0.03$	1.87	1.75	1.76	1.71	1.71	1.71
$c_{20} = 0.04$	1.88	1.74	1.74	1.72	1.77	1.76

In general, a larger c_{10} gives more mobility in the early searching stage to avoid suboptimal solutions, while a smaller c_{10} puts more weight on the ensemble-consideration refractivity $\bar{N}^{\text{EC}}$. A smaller c_{20} forces the searching process to move in a smaller step, but the searching process may stall if c_{20} is too small.

Figure 9 shows the percentage error, $100 \times (N^{\text{re}} - N^{\text{tar}})/N^{\text{tar}}(\%)$, at (0°N, 0°E), (30°N, 0°E) and (60°N,0°E), respectively, at 00:00 UTC, Jan. 1, 2013. The black line at each height level indicates an

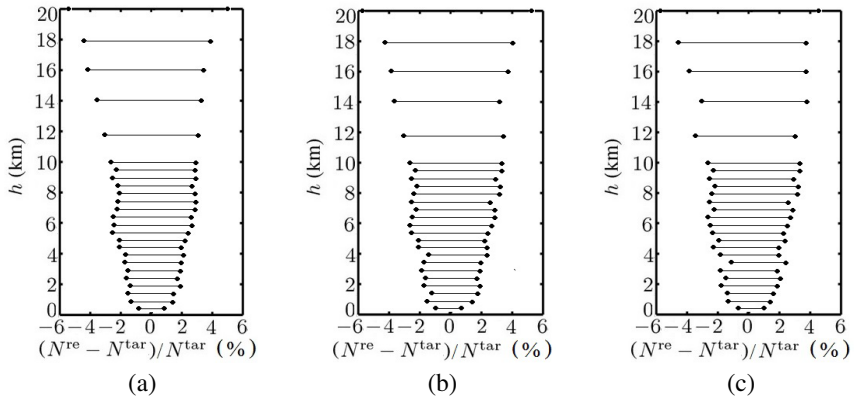

Figure 9. Percentage error, $100 \times (N^{re} - N^{tar})/N^{tar}(\%)$, by using HS-EC algorithm, (a) (0°N, 0°E), (b) (30°N, 0°E) and (c) (60°N, 0°E).

error range derived over 100 realizations. The error range is $[-2.5, 2.5]\%$ below 10 km, and increases to $[-6, 6]\%$ at altitude of 20 km. The absolute errors are smaller than 7 N-unit at all heights. As a comparison, the absolute error was about 10 N-unit in the lower troposphere when the ES method was applied [18].

6. CONCLUSION

A harmony search algorithm with ensemble consideration (HS-EC) based on atmospheric physics is applied to retrieve the refractivity profile in a specific area, from 0 to 95 km above the ground. Compared to conventional ground-based GPS retrieval techniques, the proposed method can retrieve more accurate refractivity profile partly because the upper bound of integration is extended to 95 km, and the measurement data at ground level are included. The ensemble consideration constrains the solution profile to resemble a standard profile, effectively guiding the solution from being trapped in suboptimal solutions, which may happen with the exhaustive search method or conventional HS algorithm, especially when the number of unknowns is large. The proposed method is capable of retrieving the refractivity profiles with a wider range of height and smaller height intervals, making regional weather studies more practical.

ACKNOWLEDGMENT

This work is sponsored by the Ministry of Science and Technology, Taiwan, ROC, under contract NSC 102-2221-E-002-043 and the Ministry of Education, Taiwan, ROC, under contract 105R3401-2.

REFERENCES

1. Liou, Y. A., A. G. Pavelyev, S. F. Liu, A. A. Pavelyev, N. Yen, C. Y. Huang, and C. J. Fong, "FORMOSAT-3/COSMIC GPS radio occultation mission: Preliminary results," *IEEE Trans. Geosci. Remote Sensing*, Vol. 45, No. 11, 3813–3826, Nov. 2007.
2. Chiu, T. C., Y. A. Liou, W. H. Yeh, and C. Y. Huang, "NCURO data-retrieval algorithm in FORMOSAT-3 GPS radio-occultation mission," *IEEE Trans. Geosci. Remote Sensing*, Vol. 46, No. 11, 3395–3405, Nov. 2008.
3. Kursinski, E. R., G. A. Hajj, W. I. Bertiger, S. S. Leroy, T. K. Meehan, L. J. Romans, et al., "Initial results of radio occultation observations of Earth's atmosphere using the global positioning system," *Science*, Vol. 271, No. 5252, 1107–1110, Feb. 1996.
4. Xie, F., J. S. Haase, and S. Syndergaard, "Profiling the atmosphere using the airborne GPS radio occultation technique: A sensitivity study," *IEEE Trans. Geosci. Remote Sensing*, Vol. 46, No. 11, 3424–3435, 2008.

5. Healy, S. B., A. M. Jupp, and C. Marquardt, "Forecast impact experiment with GPS radio occultation measurements," *Geophys. Res. Lett.*, Vol. 32, No. 3, L03804, Feb. 2005.
6. Le Marshall, J., Y. Xiao, R. Norman, K. Zhang, A. Rea, L. Cucurull, et al., "The application of radio occultation observations for climate monitoring and numerical weather prediction in the Australian region," *Aust. Meteorol. Oceanog. J.*, Vol. 62, 323–334, Sep. 2012.
7. Yang, S. C., S. H. Chen, S. Y. Chen, C. Y. Huang, and C. S. Chen, "Evaluating the impact of the COSMIC RO bending angle data on predicting the heavy precipitation episode on June 16, 2008 during SoWMEX-IOP8," *Month. Weather Rev.*, Vol. 142, No. 11, 4139–4163, 2014.
8. Pelliccia, F., F. Pacifici, S. Bonafoni, P. Basili, N. Pierdicca, P. Ciotti, and W. J. Emery, "Neural networks for arctic atmosphere sounding from radio occultation data," *IEEE Trans. Geosci. Remote Sensing*, Vol. 49, No. 12, 4846–4855, Dec. 2011.
9. Zhang, K., T. Manning, S. Wu, W. Rohm, D. Silcock, and S. Choy, "Capturing the signature of severe weather events in Australia using GPS measurements," *IEEE Selected Topics Appl. Earth Observ. Remote Sensing*, Vol. 8, No. 4, 1839–1847, Apr. 2015.
10. Norman, R. J., J. Le Marshall, W. Rohm, B. A. Carter, G. Kirchengast, S. Alexander, C. Liu, and K. Zhang, "Simulating the impact of refractive transverse gradients resulting from a severe troposphere weather event on GPS signal propagation," *IEEE Selected Topics Appl. Earth Observ. Remote Sensing*, Vol. 8, No. 1, 418–424, Jan. 2015.
11. Chou, Y. H. and J. F. Kiang, "Ducting and turbulence effects on radio-wave propagation in an atmospheric boundary layer," *Progress In Electromagnetics Research B*, Vol. 60, 301–315, 2014.
12. Sokolovskiy, S., "Effect of super refraction on inversions of radio occultation signals in the lower troposphere," *Radio Science*, Vol.38, No. 3, 24-1-14, Jun. 2003.
13. Von Engeln, A. and J. Teixeira, "A ducting climatology derived from the European centre for medium-range weather forecasts global analysis fields," *J. Geophys. Res. Atmos.*, Vol. 109, No. D18, D18104, Sep. 2004.
14. Zuffada, C., G. A. Hajj, and E. R. Kursinski, "A novel approach to atmospheric profiling with a mountain-based or airborne GPS receiver," *J. Geophys. Res. Atmos.*, Vol. 104, No. D20, 24435–24447, Oct. 1999.
15. Flores, A., J. V.-G. De Arellano, L. P. Gradinarsky, and A. Rius, "Tomography of the lower troposphere using a small dense network of GPS receivers," *IEEE Trans. Geosci. Remote Sensing*, Vol. 39, No. 2, 439–447, Feb. 2001.
16. Nilsson, T. and L. Gradinarsky, "Water vapor tomography using GPS phase observations: Simulation results," *IEEE Trans. Geosci. Remote Sensing*, Vol. 44, No. 10, 2927–2941, Oct. 2006.
17. Lin, L. K., Z. W. Zhao, Y. R. Zhang, and Q. L. Zhu, "Tropospheric refractivity profiling based on refractivity profile model using single ground-based global positioning system," *IET Radar Sonar Navig.*, Vol. 5, No. 1, 7–11, 2011.
18. Wu, X., X. Wang, and D. Lü, "Retrieval of vertical distribution of tropospheric refractivity through ground-based GPS observation," *Adv. Atmos. Sci.*, Vol. 31, No. 1, 37–47, Jan. 2014.
19. Sokolovskiy, S. V., C. Rocken, and A. R. Lowry, "Use of GPS for estimation of bending angles of radio waves at low elevations," *Radio Science*, Vol. 36, No. 3, 473–482, May 2001.
20. Lowry, A. R., C. Rocken, S. V. Sokolovskiy, and K. D. Anderson, "Vertical profiling of atmospheric refractivity from ground-based GPS," *Radio Science*, Vol. 37, No. 3, 13-1-19, Jun. 2002.
21. Wang, H. G., Z. S. Wu, S. F. Kang, and Z. W. Zhao, "Monitoring the marine atmospheric refractivity profiles by ground-based GPS occultation," *IEEE Geosci. Remote Sensing Lett.*, Vol. 10, No. 4, 962–965, Jul. 2013.
22. Nievergelt, J., "Exhaustive search, combinatorial optimization and enumeration: Exploring the potential of raw computing power," *Sofsem 2000: Theory and Practice of Informatics*, 18–35, Springer, 2000.
23. Rocken, C., Y. H. Kuo, W. S. Schreiner, D. Hunt, S. Sokolovskiy, and C. McCormick, "COSMIC system descriptions," *Terr. Atmos. Ocean. Sci.*, Vol. 11, No. 1, 21–52, Mar. 2000.
24. Geem, Z. W., *Recent Advances in Harmony Search Algorithm*, 1–10, Springer, 2010.

25. Gaikovich, K. P. and M. I. Sumin, "Reconstruction of the altitude profiles of the refractive index, pressure, and temperature of the atmosphere from observations of astronomical refraction," *Izvestiya, Atmos. Ocean. Phys.*, Vol. 22, 710–715, 1986.
26. Kirchengast, G., J. Hafner, and W. Poetzi, "The CIRA86aQ_UoG model: An extension of the CIRA-86 monthly tables including humidity tables and a Fortran95 global moist air climatology model," *Euro. Space Agency*, IMG/UoG Tech. Rep., Vol. 8. 1999.
27. Nafisi, V., L. Urquhart, M. C. Santos, F. G. Nievinski, J. Bohm, D. D. Wijaya, H. Schuh, A. A. Ardalan, T. Hobiger, and R. Ichikawa, "Comparison of ray-tracing packages for troposphere delays," *IEEE Trans. Geosci. Remote Sensing*, Vol. 50, No. 2, 469–481, 2012.
28. Dee, D. P., S. M. Uppala, A. J. Simmons, P. Berrisford, P. Poli, S. Kobayashi, et al., "The ERA-interim reanalysis: Configuration and performance of the data assimilation system," *Q. J. R. Meterorol. Soc.*, Vol. 137, 533–597, Apr. 2011.
29. Hedin, A. E., "Extension of the MSIS thermosphere model into the middle and lower atmosphere," *J. Geophys. Res. Space Phys.*, Vol. 96, No. A2, 1159–1172, Feb. 1991.
30. Yang, S.-H. and J.-F. Kiang, "Optimization of sparse linear arrays using harmony search algorithms," *IEEE Trans. Antennas Propagat.*, Vol. 63, No. 11, 4732–4738, Nov. 2015.
31. Jacobson, M. Z., *Fundamental of Atmospheric Modeling*, Cambridge Univ. Press, 2005.
32. Ratnaweera, A., S. Halgamuge, and H. C. Watson, "Self-organizing hierarchical particle swarm optimizer with time-varying acceleration coefficients," *IEEE Trans. Evolution. Comput.*, Vol. 8, No. 3, 240–255, Jun. 2004.
33. Hajj, G. A., E. R. Kursinski, L. J. Romans, W. I. Bertiger, and S. S. Leroy, "A technical description of atmospheric sounding by GPS occultation," *J. Atmos. Solar-Terr. Phys.*, Vol. 64, No. 4, 451–469, 2002.
34. Geem, Z. W., "Optimal cost design of water distribution networks using harmony search," *Eng. Optim.*, Vol. 38, No. 03, 259–277, 2006.